Received: 26 October 2023 | Revised: 15 January 2024 | Accepted: 18 January 2024 | Published online: 2 February 2024

RESEARCH ARTICLE

Journal of Optics and Photonics Research
2024, Vol. 1(3) 109–123
DOI: 10.47852/bonviewJOPR42021952

BON VIEW PUBLISHING

Unveiling Impact of Electron Beam Optics on Weld Attributes in EN30B Steel

Vasundhara Singh[1],* , Gour Gopal Roy[1] and Prakash Srirangam[2]

[1]*Department of Metallurgical and Materials Engineering, Indian Institute of Technology Kharagpur, India*

[2]*Warwick Manufacturing Group, University of Warwick, UK*

Abstract: The influence of electron optics in terms of beam oscillation (BO) has been studied on weld quality of several steels and reported to develop cosmetic weld with smooth surface and enhanced weld properties. However, effect of electron BO on the weld quality of medium carbon low alloy steel, especially EN30B, has not reported well and investigated in this study. By manipulating magnetic lens in-line with electron beam, the diameter of oscillating beam (OD) and its effect on weld quality has been studied. The OD was changed between 0.5 mm and 2 mm. Numerous tests, including X-ray diffraction, scanning electron microscopy (SEM), Electron Backscattered Diffraction (EBSD), hardness, wear, and tensile, were used to characterize the weld quality. Welds with BO significantly lowered the heat input rate than welds without oscillation. In presence of BO, retained austenite (RA) in the weld increased and it became least in welds made without BO. Tensile residual stress was found in the fusion zone (FZ) and it was higher with BO, especially with higher OD. In contrast to columnar grains predominantly found in welds made without BO, significant equiaxed grains were identified in welds made with BO. Nonmetallic inclusions (NMIs) in the weld became finer and less by use of BO. Introducing BO enhanced the hardness and reduced wear rate of weld, particularly at greater beam OD. Although weld strength was diminished in comparison to the base metal (BM), BO increased the weld's ductility and strength.

Keywords: EN30B steel, nonmetallic inclusions (NMIs), electron beam welding (EBW), mechanical properties, beam oscillation (BO)

1. Introduction

Medium carbon low alloy Ni-Cr-Mo steels is a European grade (EN) steel with excellent hardenability, tensile strength, and toughness. They are used in machine component members, gears, shafts, heavy-duty construction tools, rock drilling bit bodies, down hole tools, and so on [1–5]. Electron beam welding (EBW) is characterized by minimal contamination and heat damage to the material. To ascertain how EBW parameters affect the microstructure and characteristics of alloy steel components, numerous investigations have been conducted [6–8].

In the EBW weld zone, the hardenability and susceptibility to cracking of numerous hardenable plain C steels (particularly Ni-Cr, Cr-Mo, and Ni-Cr-Mo steels) were studied [9]. The main source of the cracks in the weld zone was solidification shrinkage, except for the crack that formed at the prior austenite grain boundary, where the hardness is exceptionally high. In order to study the fracture behavior of laser-welded Ni-Cr-Mo steel, a close relationship between penetration depth and crack length was established by Matsuda and Ueyama [10]. Wang et al. [4], Wang et al. [2], and Wang et al. [3] examined metal inert gas welding of Ni-Cr-Mo-V steel and provided a reasonable correlation for the mixed mode fatigue crack growth data. A basket-weave microstructure and acicular ferrite (AF) improved fracture resistance in weld metal. In addition, marine Ni-Cr-Mo-V steel damage tolerance was investigated. Later, the brief fatigue fracture propagation in heat-affected zone (HAZ) of Ni-Cr-Mo-V steel was examined and found to be controlled by microstructure and strength gradient [11]. The strain was localized by lathy borders and sub-grains.

EBW of S960M steel was studied, and it was found that the auto-tempered martensite and upper bainite dominated base metal (BM), whereas the fusion zone (FZ) and HAZ were mostly martensite, bainite, and with a little ferrite. The average hardness of fine-grained HAZ was the highest [12]. Weld tensile strength was equivalent to that of BM, 1058 MPa. HAZ and FZ possessed brittle-ductile width of 1.99 mm and 0.59 mm, respectively.

SA508Gr4 steel for nuclear pressure vessels was tested for weldability [13], and development of lath-shaped martensite in the HAZ was observed. It was also discovered that a steel vessel with a cooling period of less than 15 seconds exhibited widespread hardening and cold cracking. However, when the cooling period exceeds 1200 seconds, cracking was reduced due to the production of bainite. The research recommended preheating the workpiece to 196°C or higher to generate HAZ without cracks.

It was reported by Kar et al. [14] that dissimilar EBW joints between stainless steel and copper had more homogeneous, equiaxed microstructures, and random textures after beam oscillation (BO). The weld's ductility was also doubled by using BO. Nayak and Roy [15] reported that electron beam butt welds of zircaloy-4 made with BO had fine-basket weave Widmanstatten microstructure in the FZ, making a stronger weld. Wang and Wu [16] reported that compared to a circular oscillating electron beam, a linear oscillating electron beam produces a more refined FZ

*Corresponding author: Vasundhara Singh, Department of Metallurgical and Materials Engineering, Indian Institute of Technology Kharagpur, India. Email: vasuhappy@iitkgp.ac.in

microstructure. Wang et al. [17] demonstrated that the joints produced by a faster welding speed resulted in a finer microstructures with a higher tensile strength. They produced a correlation between travel speed and an increase in Young's modulus and hardness. Doong et al. [18] found that the use of BO greatly decreased the porosity content of 4130 steel joints and increased their fatigue life. In another work by Xia et al. [19], the application of BO for welding austenitic SS was described, in which BO formed homogenous microstructure with equiaxed grains advancing toward the center.

Nonmetallic inclusions (NMIs) and the weldability of steel have been researched. At lower heat input (120 kJ/cm), Al-Mg-Ti-O-Mn-S composite inclusions functioned as effective sites for nucleation of AF; however, at greater heat input (250 kJ/cm), this was not observed. TiN was found to be a stable inclusion in high strength low alloy steels at high temperatures reducing austenite grain size by pinning the grain boundary [20–23] reported that in low alloy steel welds the sequence of oxidation was very complex and did not follow any fixed pattern. The oxide inclusion formation depended upon alloy composition and was very sensitive to small changes in elemental concentration. The oxide inclusion formation start temperature also depended on the composition of the weld metal. Shim et al. [24] investigated the potential of various NMIs for nucleation of intergranular ferrite in manganese containing steel. Ti_2O_3 showed greater efficiency in inducing intergranular ferrite. MnS and Al_2O_3 in steel containing *V* and *N* also found to be effective to promote intergranular ferrite formation. Vargas Cortés et al. [25] reported degradation of the weld for resistance spot welded TRIP steels due to NMI generation and retained austenite (RA) degradation. It was reported that NMI increased in the weld but decreased in the HAZ. Weld properties deteriorated due to NMI but more due to decomposition of RA.

The mechanical and microstructural properties of the weld zone of DMR-29A after multi-pass gas tungsten arc welding (GTAW) and gas metal arc welding (GMAW) were studied by Venkatesh Kannan et al. [26]. The authors observed a higher volume fraction of AF in the GTAW weld zone than in the GMAW weld zone which resulted in higher strength and toughness. This was attributed to higher levels of Mn, S, and O, in observed inclusion in GTAW than GMAW, and precipitation of secondary phases favored the nucleation of AF.

It is evident from previous research that several experiments on EBW of various alloys with and without oscillating beams have been done. However, relatively little study has been published on the EBW of MCLA, especially EN30B with oscillating beams. The purpose of this study is to determine how EBW with and without BO affects the inclusions, microstructure, and properties of EN30B steel.

2. Experimental

2.1. EBW and electron optics

EBW machines have a gun chamber, work chamber, electromagnetic focusing lens, deflection cum oscillating lens, vacuum systems for both chambers, high voltage power supply, and SCADA monitor. Gun chambers have cathodes, anodes, focusing lenses, and deflection coils as shown in Figure 1(a).

EBW is made up of three functional units – beam generation, beam manipulation, and beam effect. Electrons are generated at tungsten carbon cathode by joule heating. Varying acceleration voltages, the electrons can accelerate to a speed of up to 2/3 the speed of light as they move toward the anode. The potential difference between the anode at earth potential and the negatively charged cathode creates the electric field. The voltage of the

Figure 1
Schematic representation of (a) Machine set up, (b) Types of beam oscillation of EBW machine (wave function), and (c) Sample dimension of EN30B steel

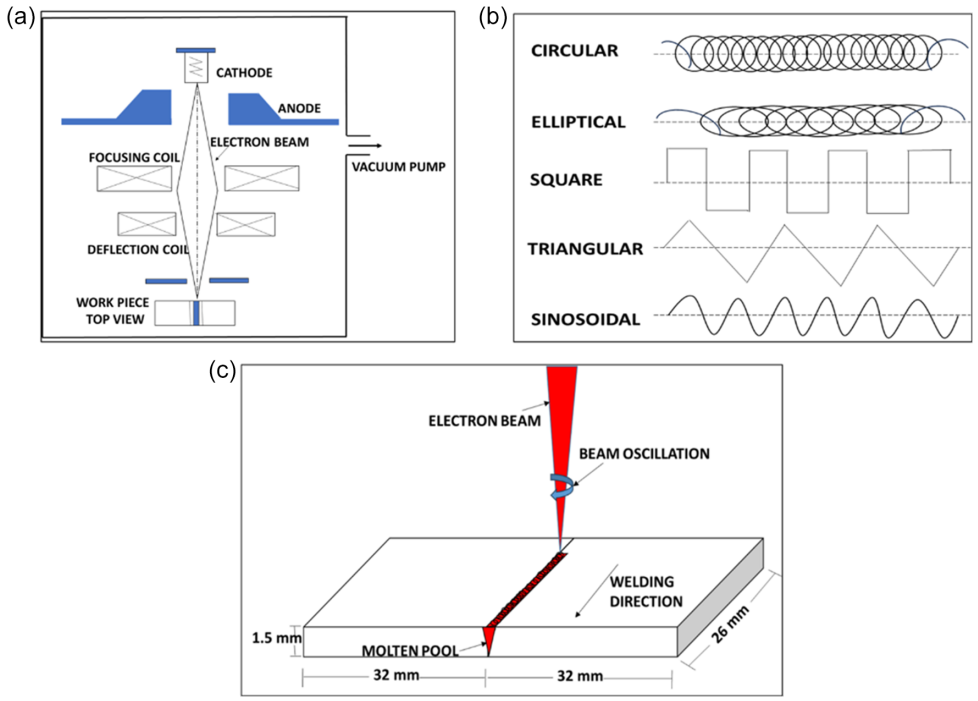

negatively charged control electrode can affect the electron beam's intensity (relative to the cathode). Through the anode bore, the electrons exit the beam generator area as a bundled electron beam that travels through several electro-optical systems. These devices have the ability to deflect the electron beam from the beam axis statically or dynamically as needed, and to shape and focus the beam as it approaches the workpiece in accordance with the requirements of the particular application.

The beam path is enclosed by the focusing coil (or focusing lens ring-shaped)'s wire windings and high-permeability iron on three sides. The focusing coil's magnetic field acts as a lens when powered. The EB is a cone protruding from its apex. Lorenz force drives electro-optical systems, which describes the behavior of electrons as they traverse an electromagnetic field. The intensity of the electromagnetic field is determined by the direct current (lens current) passing through the ring coil; consequently, this intensity impacts the Lorentz force exerted on every electron within the electromagnetic field. By manipulating the lens current, it is possible to concentrate electrons on different working heights or perform welding in the defocused region.

A beam deflection mechanism is positioned underneath the focusing lens. Four pairs of alternately connected coils wrap an iron core. The coil pairs are coaxial along the beam path, whereas the deflection mechanism is orthogonal along the major axes *X* and *Y*. Two coils form an electromagnetic field that deflects the beam from the beam axis when current flows. A function generator and amplifiers control both pairs of coils to beam deflection at any angle between the major axes at constant current flow. BO is possible with dynamic alternating currents supplied to coils. Various types of BO available are shown in Figure 1(b). In the present study, circular BO has been studied.

Figure 1(c) depicts the schematics for a butt-welding configuration of EN30B steel. Butt welding was prepared using an 80 kV, 12 kW using EBW machine at the Bhabha Atomic Research Center, Department of Atomic Energy, India. The EBW process variables used here for EB welding were vacuum gun chamber (mbar) = 10^6, vacuum chamber for welding (mbar) = 10^5, and distance of gun specimen (mm) = 465. Circular motion has been introduced to the BO during EBW. The work distance was 200 mm. Table 1 lists the EBW-operating conditions including BO used in the present study.

2.2. Materials and characterization techniques

EBW was carried out on forged EN30B steel sample, which is the BM of dimensions (mm^3) = 32 × 26 × 1.5. Chemical analysis of the after forged BM sample used in the current study is shown in Table 2. After butt welding, the sample dimension (mm^3) was 64 × 26 × 1.5 (L × B × H).

For microstructure analysis, the sample was prepared transverse section of the weld specimen. These samples were polished using different grades of emery paper followed by cloth and diamond polishing, to give a mirror finish. Then they were etched chemically using Vilella's reagent (100 ml ethanol + 5 mL HCL + 1 g picric acid). To reveal prior austenite grains, some samples were etched with hot picric acid etchant (2% picric acid in 10 ml distilled boiled water with 2–3 drops of HCL, and soap solution). For morphological study, the samples were then observed under optical microscope (Leica DM 2500 M microscope). Under detailed microstructural investigations, the samples were polished to 0.05 μm and seen under SEM JEOL (using JSM-IT300HR-JEOL). For compositional microanalysis, energy dispersive spectroscopy (EDS) was done, using X-ray probe attached to the SEM machine.

EBSD studies were performed at a step size of 0.2 μm using TSL OIM analysis software (fitted in Zeiss® Auriga compact dual beam scanning electron microscope) from Oxford Instruments, UK, operated at 20 kV over the sample before and after EB welding. The samples were mounted with a 70º tilt position relative to the main beam with a 15 mm working distance in the FESEM specimen chamber. The sample surfaces of EBW joints were gently polished with aqueous colloidal silica solution before EBSD scanning. The sample surfaces, after hot compression tests, were electrolytically polished in a solution of 30 vol. % of perchloric acid and 70 vol. % acetic acid at 20 volts and 15 seconds. EBSD was performed at a flat and electro-polished (with solution) surface of the sample.

Wilson hardness testing machine measured weld bead, HAZ, and FZ transverse hardness. Averaging ten indentations in each location yielded Vickers hardness (HV) with a standard deviation of ±5 for each example. For room-temperature tensile test, tensile specimens were prepared on a transverse section perpendicular to the welding direction using wire EDM according to standard ASTM E8/E8M as seen in Figure 2. The tensile test was carried out (SHIMADZU: AG-5000G) on universal testing machine, using a 10 kN maximum

Table 1
The operating parameters for welds with and without beam oscillations

No.	Sample ID	Travel speed (S) (mm/min)	Voltage (V) (kV)	Current (I) (mA)	With beam oscillation: Oscillation diameter (OD) (mm)	With beam oscillation: Oscillation frequency (Hz)	Without beam oscillation (WO)
1.	S1000V60I15OD 2 mm	1000	60	15	2	300	No
2.	S1000V60I15OD 0.5 mm	1000	60	15	0.5	300	No
3.	S1000V60I15 WO	1000	60	15	–	–	Yes

Table 2
Chemical composition of the investigated EN30B steel in wt. %

Elements	C	Si	Mn	Ni	Cr	Mo	S	P	Al	Fe
Composition (Wt. %)	0.31	0.24	0.48	4.21	1.24	0.25	0.02	0.025	0.013	93.21

Figure 2
Tensile specimen dimension for EN30B steel

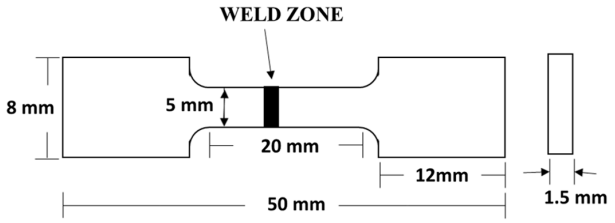

load capacity and a 0.2 mm/min digital extensometer. Tests were performed three times for each weld condition in order to obtain mean results with a ±5 standard deviation.

Diffraction using a Bruker D8 Discover X-ray diffractometer was used to measure RA and residual stress for welds with different settings. Selected incident X-ray was Co-K radiation (wavelength: 1.789). A ball-on-disk wear tester was employed (MFT-5000 Tribometer, Manufacturer: RTEC INSTRUMENTS INC. with Serial no. ETEC2659). The wear test was performed at 30 N, 30 min, 10 Hz, and 2 mm stroke length. Testing was conducted three times per weld condition, with an average standard deviation of ±5.

3. Results and Discussion

3.1. Heat input calculation for different welding conditions

Heat input rate (kJ/cm) is an important parameter to understand microstructure evolution in the weld. During BO, the heat input rate is likely to increase manifold as the heat source traverses a longer distance to cross the same distance in the welding direction. Therefore, before discussing the evolution of microstructure and weld properties, we have calculated the heat input rate during welding, both with BO and without BO, and detailed below.

Heat input per unit length (Q, kJ/cm) is computed using Equation (1):

$$Q = \eta \frac{V * I}{v} \quad (1)$$

where V and I are voltage and beam current, respectively.

η represents the efficiency of power supply (~ 0.95),

v is the travel speed of the beam, mm/min.

The beam travel speed and welding speed are equal when there is no oscillation. Depending on the welding speed and the oscillation settings, the electron beam's velocity can fluctuate during BO and reach several thousand mm/s (OD and frequency). According to reports in the literature, the velocity of the circular oscillating beam is determined using Equations (2–4) [27].

$$v = \sqrt{{v_x}^2 + {v_y}^2} \quad (2)$$

$$v_x = \frac{dx(t)}{dt} = 2.\pi.f_x.a_x.\cos\cos\left(2\pi f_x t + \Phi_x\right) \quad (3)$$

$$v_y = \frac{dy(t)}{dt} = v_w + 2.\pi.f_y\,a_y.\cos\cos\left(2\pi f_y t + \Phi_y\right) \quad (4)$$

where the oscillation amplitude and frequency, respectively, are denoted by the letters a and f.

The initial phase angle is represented by Φ. The x- and y-components are denoted by the subscripts x and y, respectively. The phase shift is π/2, when A frequency and amplitude are equivalent. And the welding scan velocity is denoted by v_w.

Heat input values with and without BO are shown in Table 3. Table 3 also shows weld bead thickness, which increases with heat input.

Table 3
Comparisons of the heat input calculated from the measured weld bead for each of the weld parameters for EN30B steel

S. No.	Sample ID	Measured weld bead (FZ) (mm)	Calculated Q (kJ/cm)
1.	S1000V60I15 OD 2 mm	2.170	0.05
2.	S1000V60I15 OD 0.5 mm	2.2569	0.18
3.	S1000V60I15 without BO	2.334	0.855

3.2. Macroscopic study after welding with FZ, HAZ, and BM for EN30B steel

Figure 3 depicts the appearance of weld beads in cross-section under three different welding settings. Figure 3(a) and (b) depicts the welds produced with BO, which demonstrate almost a defect-free welding, except some undercut at the top. Welding without BO does not show any undercuts but resulted in massive crack propagation from the bottom to the center of the weld, as illustrated in Figure 3(c). BO induces heat mixing in the weld seam by creating churning action, reduces unidirectional temperature gradients, and associated thermal stress, reducing the chances of crack formation. However, a mild crack from bottom to the center in case of weld produced with BO at lower OD might be inefficient fluid and heat mixing in the weld seam. The undercut at the top surface of the weld with BO may be attributed to lower heat input and insufficient heat and lack of melting.

The SEM microscopy characterization of the FZ further clarifies the cracks in the welds, as shown in Figure 4. EDS analysis also revealed the presence of some intermetallic compounds in the cracked region of EN30B steel. The intermetallics observed were Ni_3Al, and some NMIs Al_2O_3, and MnS were also observed in the crack region. It indicates that intermetallics and inclusions acted as stress concentrators, and cracks are formed by releasing the stress.

Figure 5 shows optical pictures of EN30B steel following hot picric acid etching to get prior austenite grain boundaries. It is found that prior austenite grains were largely columnar in welds produced without BO (Figure 5(c)), and those were equiaxed dendritic in case of welds produced with BO, especially with 2 mm and 0.5 mm OD (Figure 5(a) and (b)). Equiaxed dendritic grains may be promoted by a low G/R, where, G represents temperature gradient, and R the speed of solidification. Low heat input during BO produces faster cooling rate or solidification rate. Low temperature gradient, on the other hand, may be promoted by churning action and heat mixing during BO [14, 15]. Figure 5(d) shows the largest grain size for the BM case.

Figure 3
Macro images show the appearance of weld beads in cross-section under various weld conditions (a) S1000V60I15 OD 2 mm, (b) S1000V60I15 OD 0.5 mm, and (c) S1000V60I15 without BO

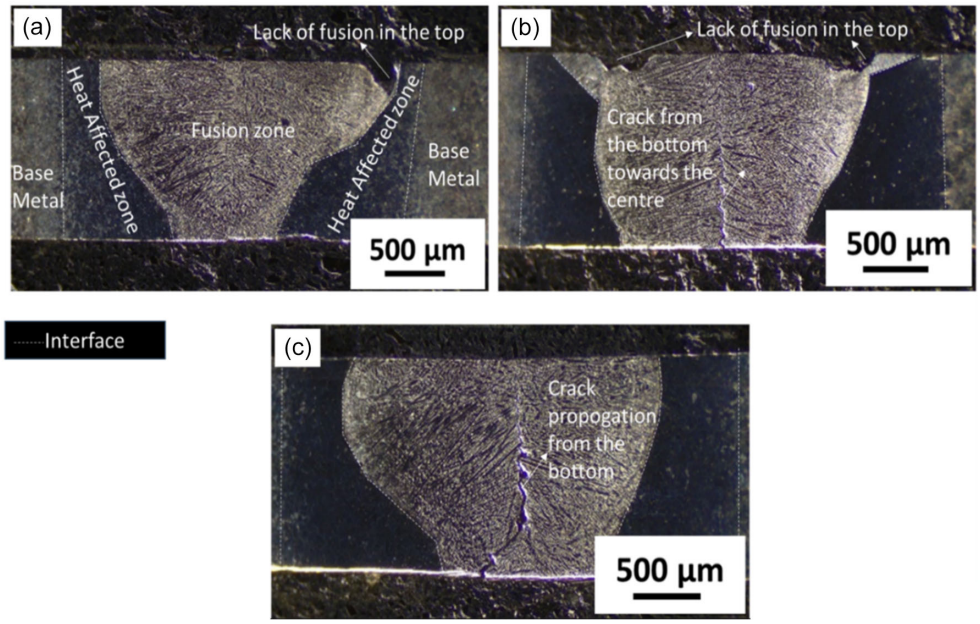

Figure 4
Optical images at 5X magnification are presented for different welding conditions (a) S1000V60I15 OD 2 mm, (b) S1000V60I15 OD 0.5 mm, (c) S1000V60I15 without BO, (d) Shows magnified cracked region with point EDX mapping, and (e) Represents the point EDX and area mapping

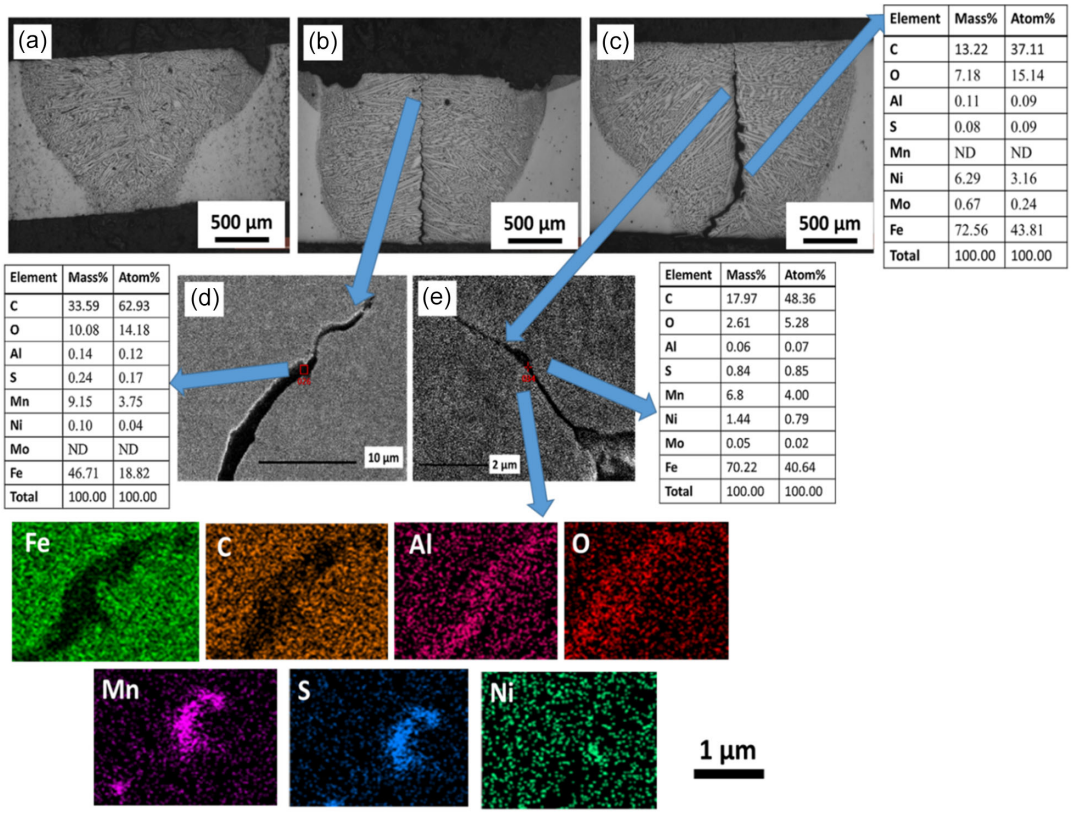

Element	Mass%	Atom%
C	13.22	37.11
O	7.18	15.14
Al	0.11	0.09
S	0.08	0.09
Mn	ND	ND
Ni	6.29	3.16
Mo	0.67	0.24
Fe	72.56	43.81
Total	100.00	100.00

Element	Mass%	Atom%
C	33.59	62.93
O	10.08	14.18
Al	0.14	0.12
S	0.24	0.17
Mn	9.15	3.75
Ni	0.10	0.04
Mo	ND	ND
Fe	46.71	18.82
Total	100.00	100.00

Element	Mass%	Atom%
C	17.97	48.36
O	2.61	5.28
Al	0.06	0.07
S	0.84	0.85
Mn	6.8	4.00
Ni	1.44	0.79
Mo	0.05	0.02
Fe	70.22	40.64
Total	100.00	100.00

Figure 5
Optical images 20X magnification for welding parameters (a) S1000V60I15 OD 2 mm, (b) S1000V60I15 OD 0.5 mm, (c) S1000V60I15 without BO, and (d) BM

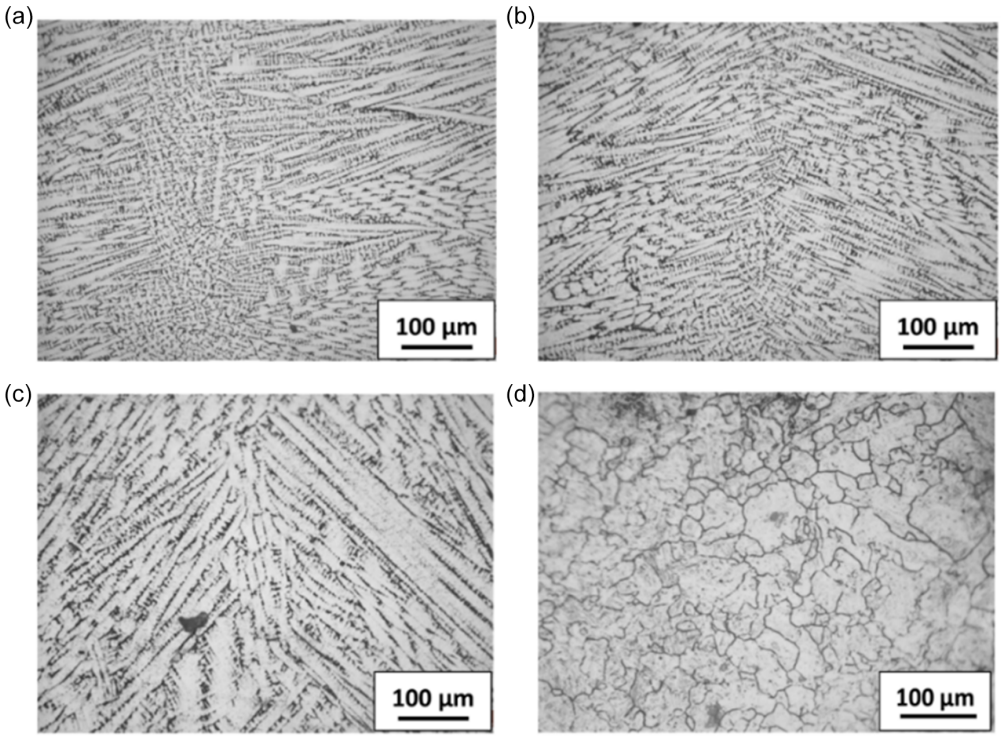

3.3. Analysis of the welded region by EBSD

Figure 6 depicts the IPF maps of welds zone. Figure 6(a) shows that finer grains are prevalent in the weld zone prepared with a BO at OD of 2 mm. For a BO diameter of 0.5 mm in Figure 6(b), grains got slightly coarser, and for a without BO condition as seen in Figure 6(c), grains became even coarser. The grains become coarser with increase in the heat input, or decrease in cooling rate for different welding conditions, as presented in Table 3. Besides, BO induces heat mixing in the weld [14, 15] which reduced unidirectional temperature gradients, and multidimensional grain growth, and consequently equiaxed smaller grains.

The phase mapping of the welded samples is shown in Figure 7. For various welding conditions, the proportion of austenite and ferrite varied. The quantity of residual austenite was highest (5.20%) for weld produced with BO at 2 mm OD as seen in Figure 7(a). For welding without BO, it was the lowest at 0.7% as seen in Figure 7(c). It was intermediate for weld produced with BO at OD of 0.5 mm as seen in Figure 7(b). Similar phase quantification was also done under Rietveld analysis of X-ray diffraction (XRD) data, discussed in a following section.

Figure 8 displays the grain size distribution for each sample condition. It demonstrates that grain refining occurs under BO and refining was maximum for larger OD (2 mm) (as seen in Figure 8(a)) followed by increasing grain size with increase in cooling rate (as seen in Figure 8(b)), as a result of the maximum cooling rate and the lowest heat input. However, grain coarsening was noticed particularly with higher heat inputs for welding without BO (as seen in Figure 8(c)). For BM grain, size is highest (as seen in Figure 8(d)).

Figure 9 displays the grain misorientation plot for each sample condition. It demonstrates that the highest average misorientation fraction occurs under BO (as seen in Figure 9(a) and (b)), and it is maximum at the largest BO diameter. This can be attributable to the rapid cooling rate and minimal heat input, resulting in local strains in the grains. On the other hand, the weld produced without BO at the slowest travel speed showed the least grain misorientation (as seen in Figure 9(c)). BM had lowest grain orientation (as seen in Figure 9(d)).

3.4. Phases, residual stress, lattice strain, and dislocation density from XRD analysis

The XRD patterns of the EN30B steel for both with BO, without BO, and actual BM are seen in Figure 10(a), (b), (c), and (d). According to the XRD, the weld contains both the FCC (RA) and BCC (ferrite/martensite) phases. Welds produced without BO had less RA phase than those produced with BO. When the OD was reduced from 2 mm to 0.5 mm, there was a reduction in the amount of austenite phase (as seen in Figure 10(a) and (b)). The RA amount in the weld was also estimated by Rietveld analysis of the XRD data. These values for weld produced with BO at 2 mm OD, 0.5 mm OD, and without BO were 4.8%, 1.63%, and 0.3%, respectively. It may be noted that these estimations closely follow the estimation by IPF map study (Figure 6(a), (b), and (c)). BO brings in churning action, heat mixing [15, 28] reducing the unidirectional temperature gradient and thermal strain, which is expected to restrict the strain-induced phase transformation (austenite to martensite). As a result, RA is seen more significantly in the beam-oscillated weld seam, particularly for

Figure 6
IPF maps for welding parameters (a) S1000V60I15 OD2 mm, (b) S1000V60I15 OD 0.5 mm, and (c) S1000V60I15 without BO

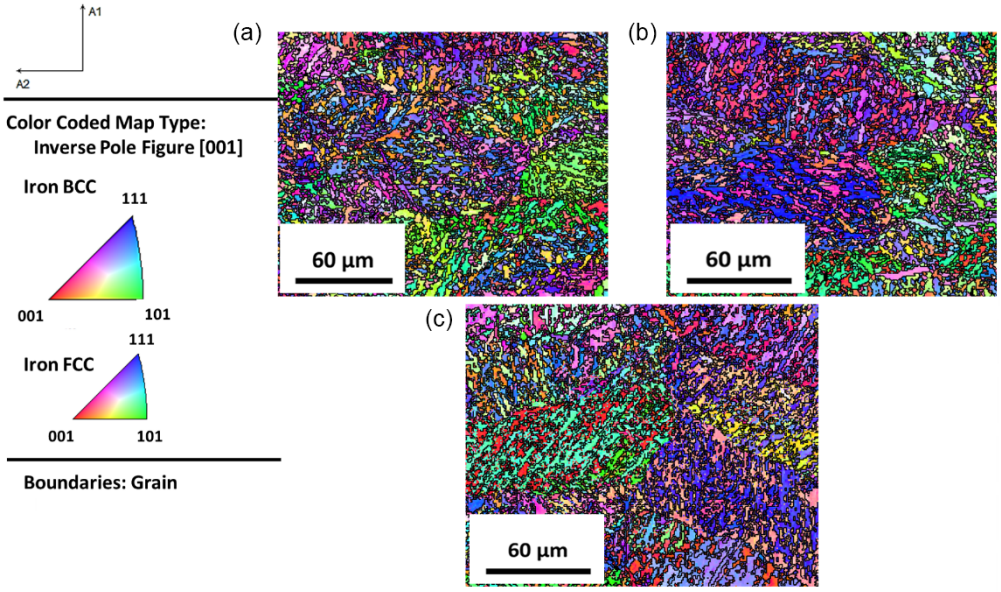

Figure 7
Phase maps for (a) S1000V60I15 OD 2 mm, (b) S1000V60I15 OD 0.5 mm, and (c) S1000V60I15 without BO

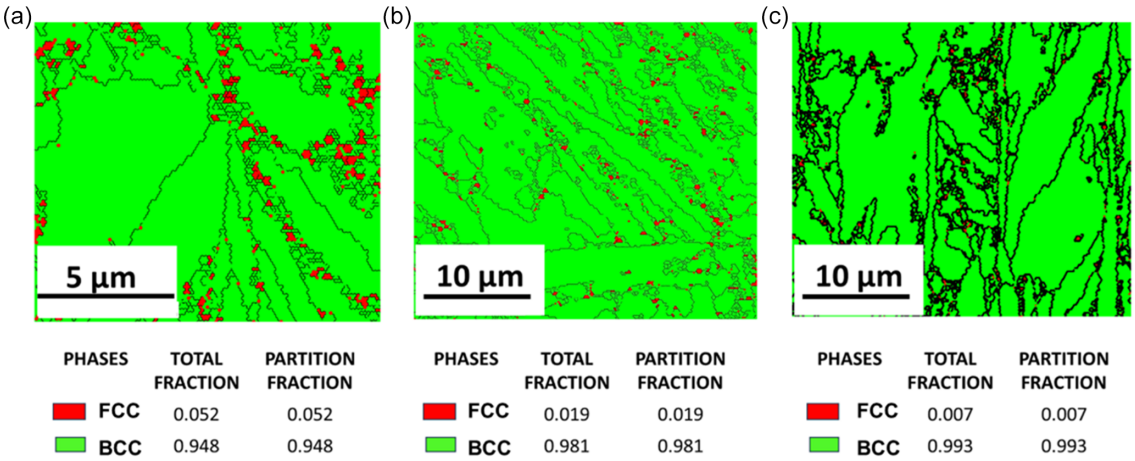

large OD. For all welding situations, whether they involved BO or not, intermetallic Ni_3Al is also seen.

The residual stresses of FZs were computed from XRD data [29, 30] by peak broadening analysis, as shown in Figure 11(a) and (b). The lattice strain and dislocation density plots in Figure 11(c) and (d) are computed using the Williamson–Hall method (W-H method) [31, 32].

The residual stresses, lattice strain, and dislocation density resulting from several welding conditions are illustrated in Table 4. The accompanying discussion will encompass the hardness values of the weld as well as the dimensions of NMIs. The residual stresses in the weld zone were tensile regardless of BO, whereas the BM had compressive residual stresses. The residual stress was found to be maximum for BO at the largest OD, attributed to the lowest heat input, maximum cooling rate, and higher local thermal stresses. It is also evident from higher strains and dislocation density, as shown in Figure 11(c) and (d), respectively. Similarly, the weld generated without BO had the lowest residual stress, attributed to the higher heat input and lower cooling rate, and lower thermal stress. It is also evident from lower lattice strain and lower dislocation density, as shown in Figure 11(c) and (d), respectively.

Figure 8
Variation in grain size for (a) S1000V60I15 OD 2 mm, (b) S1000V60I15 OD 0.5 mm, (c) S1000V60I15 without BO, and (d) BM

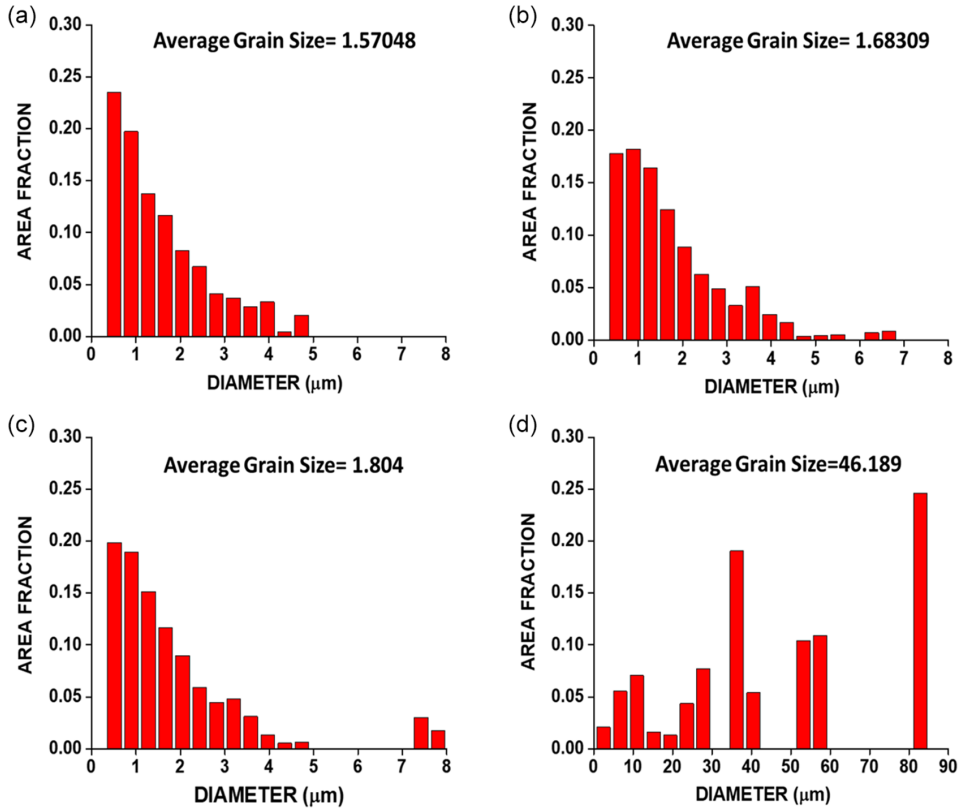

Figure 9
Misorientation plot distribution for welding parameters (a) S1000V60I15 OD 2 mm, (b) S1000V60I15 OD 0.5 mm, (c) S1000V60I15 without BO, and (d) BM

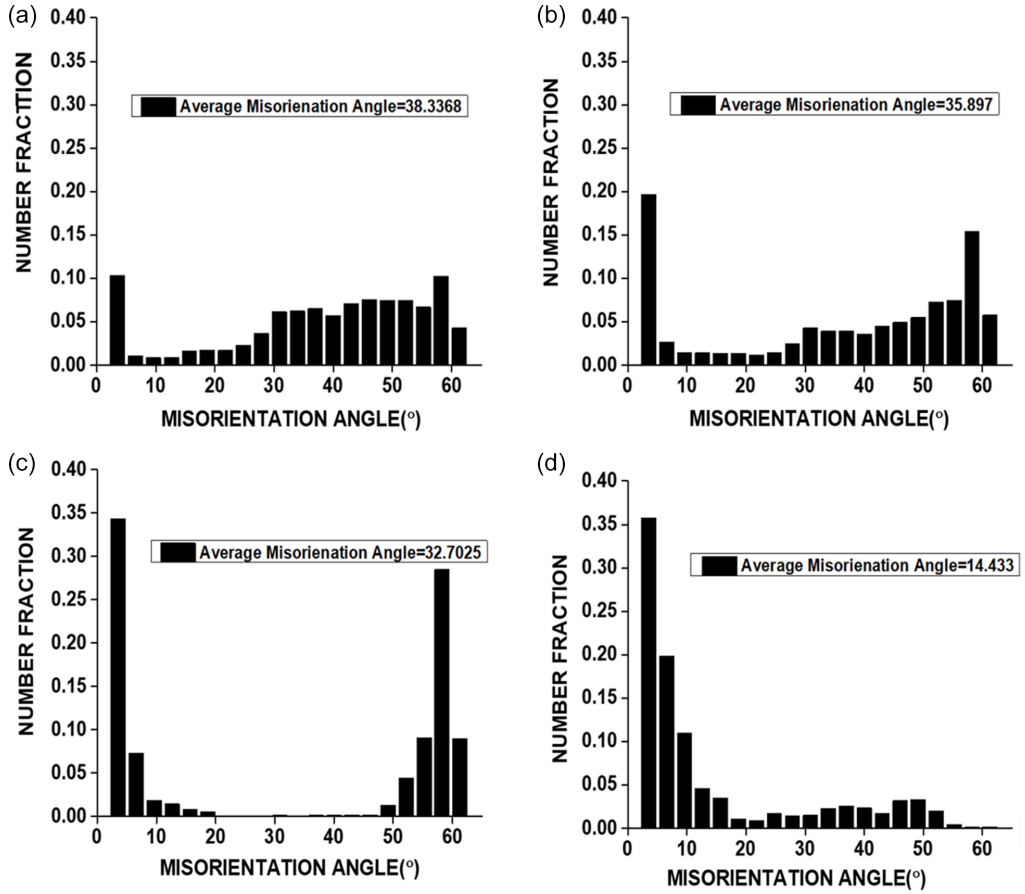

Figure 10
XRD peak for (a) S1000V60I15 OD 2 mm, (b) S1000V60I15 OD 0.5 mm, (c) S1000V60I15 without BO, and (d) BM

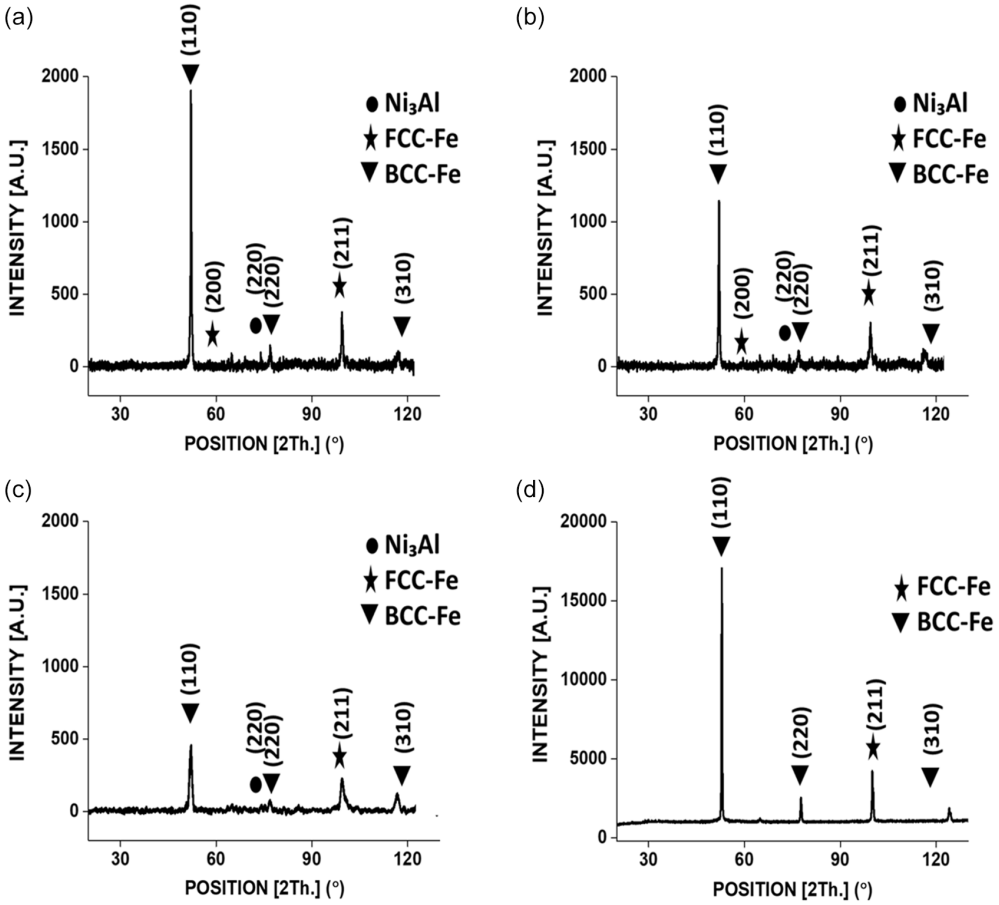

Figure 11
(a) Micro strain calculation from peak broadening, (b) Residual stress plot, (c) Lattice strain %, and (d) Dislocation density for all sample conditions

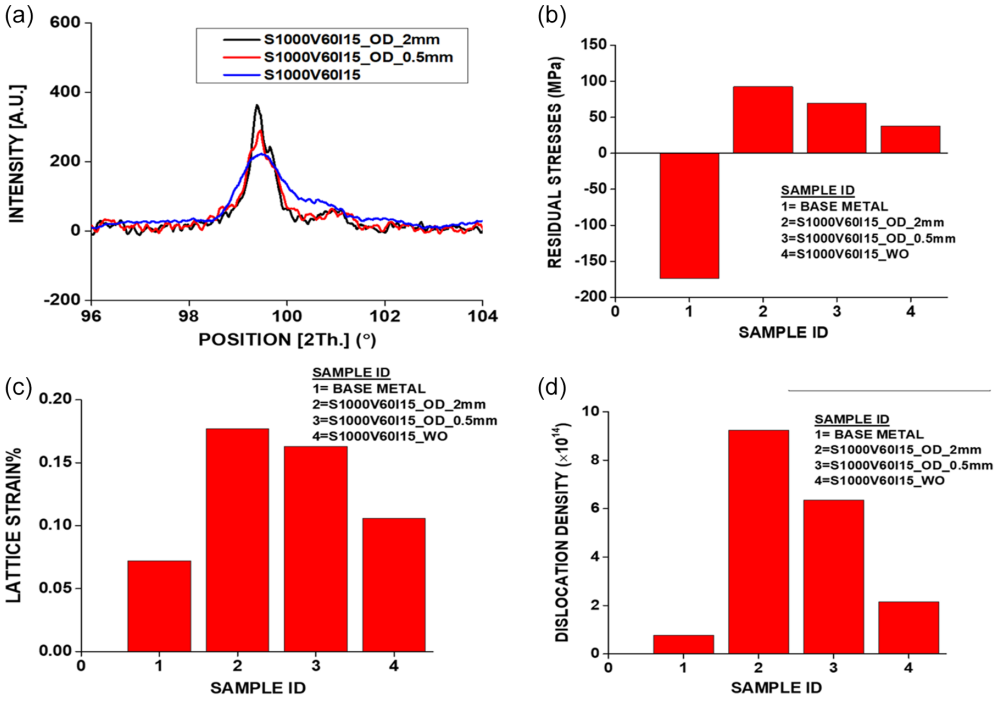

3.5. Hardness measurements

The hardness results for EBW joints under five welding settings are shown in Figure 12(a). The eleven locations in a welded sample where hardness data were extracted are shown in Figure 12(b). Vickers hardness measurements revealed that BM had the lowest hardness and that the maximum hardness was observed in FZ.

The FZ, whether prepared with or without BO, had the maximum value of hardness under all welding conditions. BM is thermo-mechanically treated and was much softer. The weld undergoes thermal cycles where heating and cooling rates are very fast, especially under EBW, producing non-equilibrium phases like intermetallic, martensite, and making it harder. Such high hardness values of HAZ and FZ well above the BM are also reported by Sharma et al. [33] and Neto et al. [34].

3.6. Tensile test

Tensile samples broke in the FZ irrespective of whether those were prepared with or without BO. UTS and ductility of the welds were much lower than that of BM (980 MPa, 20% ductility). However, the ductility of the weld improved marginally than its non-oscillating counterparts. The UTS and % elongation of the welds prepared with BO at ODs 2 mm, 0.5 mm, and weld prepared without BO were 452 MPa ± 3 with elongation 7.89% ± 2, 432 MPa ± 3 with elongation 6.7 % ± 2, and 307 MPa ± 3 with elongation 5.11% ± 2. Figure 13 shows the fractography of the fractured EB-welded tensile specimens for all three weld conditions and BM. It is seen that all fractured weld showed a brittle fracture mode, while the BM shows a ductile mode of fracture.

3.7. Wear test

Figure 14(a) shows the temporal variation of the coefficient of friction (COF). When frictional force is influenced by surface asperities of various hardness and scales, COF is defined as the ratio of frictional force to normal force. The greater the COF, the greater the amount of wear and the lower the resistance to wear. The BM has the highest COF in the range of 0.60–0.65, indicating it is more wear prone, as evidenced by the maximum wear volume and wear rate, as shown in Figure 14(b) and (c).

COF was the least for weld produced with BO at the highest OD (2 mm), followed by the weld produced by BO with a 0.5 mm OD. The weld produced without BO showed a higher COF, and corresponding higher wear volume and wear rate than its oscillating counterparts. Wear volume and the wear rate were the minimum for the weld produced with BO at a 2 mm OD. Such variation in wear rate directly corroborates with the hardness variation in Table 4; the higher the hardness, the higher is the wear resistance [35].

Table 4
Calculation of FZ residual stress, lattice strain, dislocation density, hardness, wear rate, and NMI size for different sample conditions

S. No.	Sample ID	Lattice strain %	Residual stress (MPa)	Dislocation density (mm^{-2})	Hardness of FZ (HVN)	Wear rate (10^{-4}) (mm^{-2})	NMIs size range (μm)
1.	S1000V60I15 OD 2 mm	0.177	92.7 ± 15	9.24×10^{14}	668 ± 5	0.9487	0.21–1.88
2.	S1000V60I15 OD 0.5 mm	0.163	69.55 ± 18	6.34×10^{14}	665 ± 5	1.0185	0.77–6.56
3.	S1000V60I15 without BO	0.106	37.71 ± 12	2.15×10^{14}	663 ± 5	1.3129	1.51–8.00
4.	Base metal	0.072	−174 ± 26	0.771×10^{14}	260 ± 5	1.5599	1.89–10.00

Figure 12
(a) Evaluation of the hardness of EN30B steel subsequent to multiple welding situations, encompassing BM, HAZ, and FZ and (b) Samples of EN30B welded steel at various points from which hardness measurements are obtained, beginning at point −5 and proceeding to 5 in Figure 11 (a)

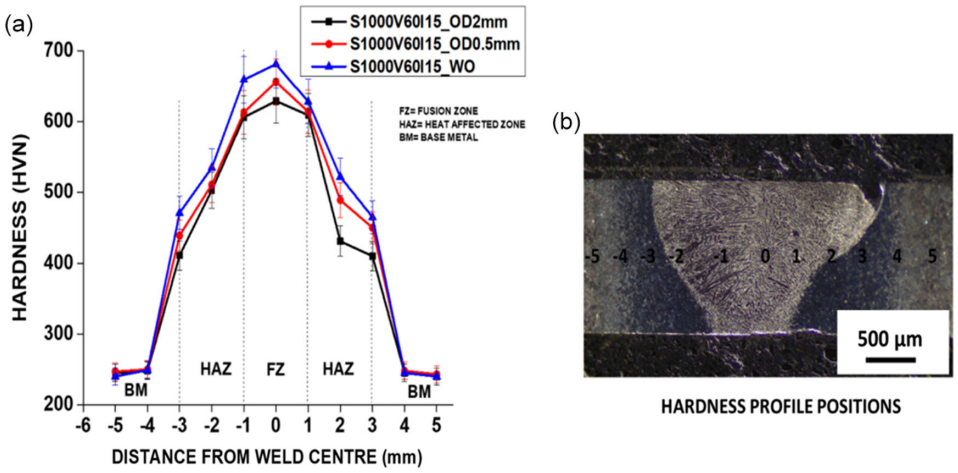

Figure 13
Fractography of EN30B steel after tensile test for different sample conditions (a) S1000V60I15 OD 2 mm, (b) S1000V60I15 OD 0.5 mm, (c) S1000V60I15 without BO, and (d) BM

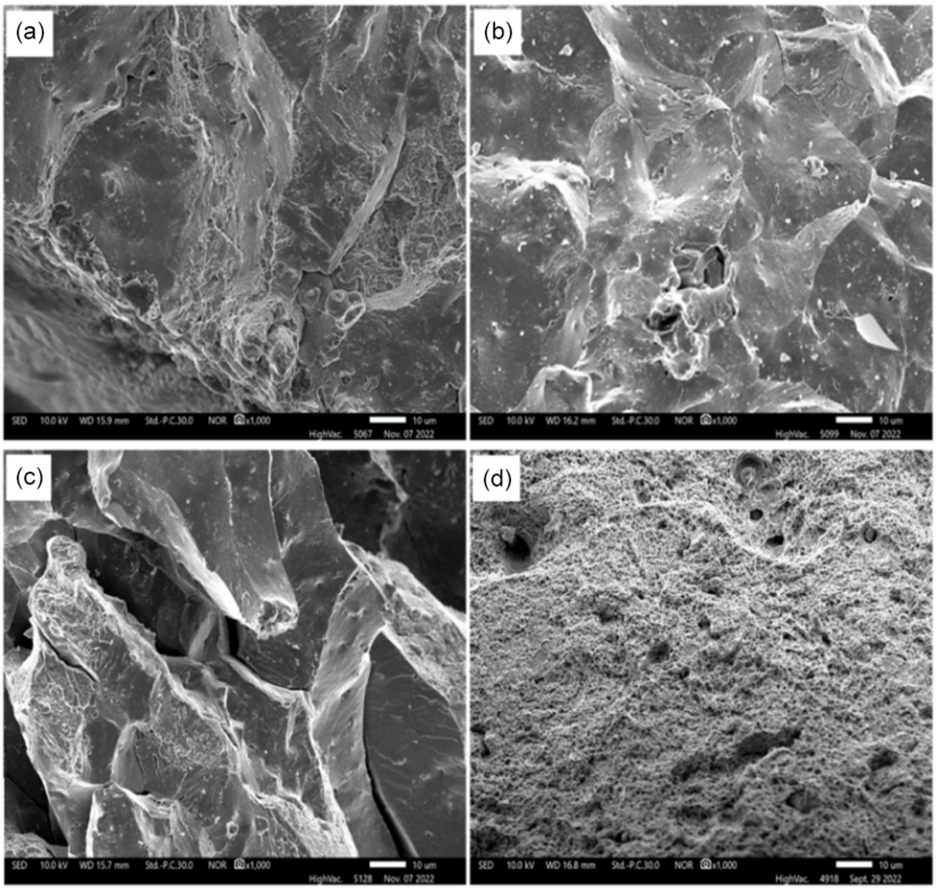

Figure 15(a), (b), (c), and (d) shows the SEM image of the wear surface of three welds and the BM. It is evident that the wear debris is minimum for weld produced with BO diameter at 2 mm and it is maximum for BM.

3.8. Study of variation of NMIs size with welding conditions

Figure 16 depicts the morphological change in the size of NMIs under various welding parameters. Figure 16(a) and (b) shows inclusions in a weld created using BO at 2 mm and 0.5 mm ODs, respectively. Figure 16(c) and (d) shows inclusions in welds produced without BO and for the BM, respectively. At a 2-mm OD, the average size of NMIs was found to be the smallest. This measurement of NMIs size was done accurately using Image J software.

Because of the relatively higher heat input and slower cooling rates in all other situations, inclusion sizes became larger. Table 4 shows the distribution of NMIs under various welding parameters. Inclusions dissolve in the matrix during heating and re-precipitate after solidification, the extent of which depends on the solidification rate. At faster solidification rates, less time is available for inclusion segregation, supersaturation, and subsequent precipitation. As a result, smaller inclusions evolve in the weld that was prepared with BO at a higher OD (2 mm), which is characterized by the lowest heat input and maximum cooling/solidification rate.

3.9. Discussion

The current study aimed to comprehend how EB welding, both with and without BO, changed the inclusions, microstructure, and characteristics of steel of the EN30B grade. The study revealed that BO during EBW enhanced the weld properties like tensile strength, ductility, wear properties, and residual stress for EN30B steel, not reported earlier. The present investigation also reports on favorable inclusion evolution during BO. BO during EB welding is a unique parameter that is reported to produce a churning action in the weld seam, resulting in a smooth cosmetic weld. Notably, it is reported to develop a more uniform and equiaxed microstructure in the weld seam, responsible for enhanced mechanical properties. However, there are a few versions of speculation about the mechanism of churning action in the weld pool, including the hypothesis of the research group, reported earlier by Kar et al. [14], Nayak and Roy [15], Wang et al. [36], and Yang and He [37]. The gist of the hypothesis is as follows. It is unlikely that the movement of a single weld pool along the path of the beam trace can bring mixing in the weld seam. Because heat input under BO is abysmally small, it could only produce a very tiny weld pool. The interaction of such tiny weld pools, which are likely to overlap significantly and intricately, could produce heat exchange very tortuously, mixing heat. Such heat mixing breaks the unidirectional temperature

Figure 14
Wear test of EN30B steel for welding parameter (a) COF vs. time, (b) Wear volume vs. time, and (c) Wear rate vs. time, all for load 30 N track length 2 mm and frequency 10 Hz

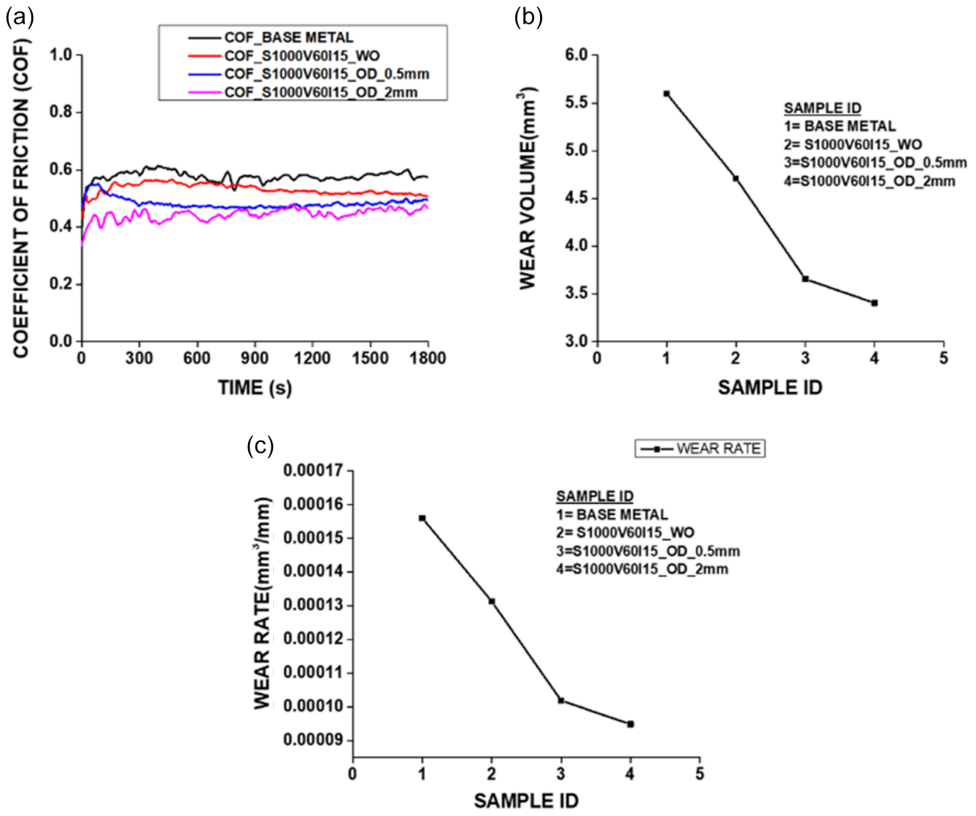

Figure 15
SEM image of wear surface of EN30B steel for weld parameters (a) S1000V60I15 OD 2 mm, (b) S1000V60I15 OD 0.5 mm, (c) S1000V60I15 without BO, and (d) BM, all for load 30 N track length 2 mm and frequency 10 Hz

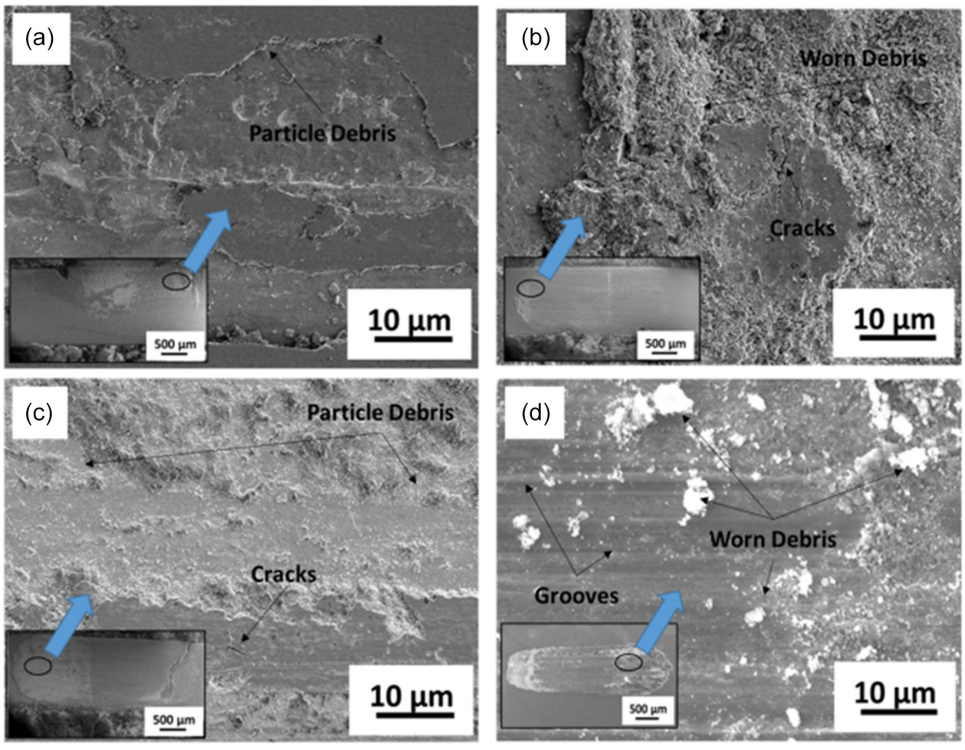

Figure 16
Nonmetallic inclusion size variation for EN30B steel under welding parameters (a) S1000V60I15 OD 2 mm, (b) S1000V60I15 OD 0.5 mm, (c) S1000V60I15 without BO, and (d) BM

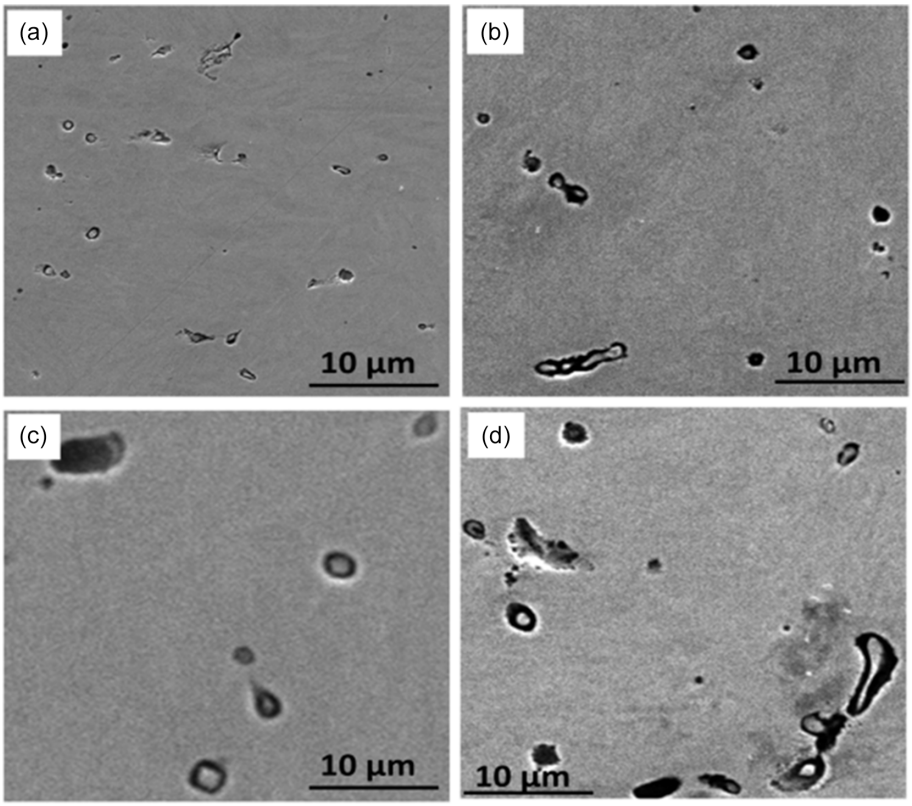

gradients and promotes the development of equiaxed refined grains and uniform microstructure.

4. Conclusion

1) Effect of electron optics in terms of BO has been studied on the weld quality of EN30B steel.
2) The heat input per unit length calculated based on analytical expression was lowest (5×10^{-3} kJ/cm) for the sample welded by BO at 2 mm oscillation diameter (OD). In contrast, it was a maximum (81 kJ/cm) for the sample welded with the un-oscillated beam.
3) The sample welded with a 2 mm beam OD had colonies of equiaxed grains at the center. It is attributed to lower *G*/*R*, produced by the churning action and better heat mixing in the weld pool, and high cooling/ solidification rate.
4) The weld produced using BO at the higher OD of 2 mm was found to have the largest fraction (5.2%) of RA, attributed to better mixing, reduced stress generation, and stress-induced transformation from austenite to martensite. The reduction in OD (0.5 mm) resulted in a decrease in the fraction of RA, whereas the sample welded with a non-oscillated beam had a minimum 0.7% RA.
5) The hardness of the weld and HAZ was much higher than the BM. The high hardness of the FZ followed by HAZ was attributed to the formation of non-equilibrium harder phases like intermetallic and martensite under faster heating and cooling under EBW.
6) The residual stress induced in the weld zone due to EBW was tensile in nature for all welding conditions as compared to compressive residual stress in the as-received samples. Residual stress was found to be highest for welds produced with BO at higher OD.
7) The application of BO leads to a significant reduction in the size of NMIs with a minimum for the sample welded with a 2 mm OD. This reduction in the inclusion size may be attributed to the inclusion dissolution and re-precipitation in the matrix constrained by rapid solidification.
8) The fretting wear resistance was found to increase after welding, and it was maximum for the samples welded with BO. This increase in fretting wear resistance was attributed to the increased hardness of the FZ due to the formation of non-equilibrium phases.
9) The UTS and % elongation of the joint decreased after welding. However, the joint prepared with BO, especially at higher oscillation diameter, produced higher strength and ductility than its non-oscillating counterpart.

Funding Support

The Department of Heavy Industry (DHI), Government of India (GOI), and Heavy Engineering Corporation Ltd. (HEC), Ranchi, extended the financial support for this project. (Sanction Number: 12/4/2014-HE&MT, Dated: November 10, 2017), Bhabha Atomic Research Center, Department of Atomic Energy, India also provided EBW facilities for carrying out experiments.

Ethical Statement

This study does not contain any studies with human or animal subjects performed by any of the authors.

Conflicts of Interest

The authors declare that they have no conflicts of interest to this work.

Data Availability Statement

Data sharing is not applicable to this article as no new data were created or analyzed in this study.

References

[1] Muthukumaran, G., Rai, A. K., Gautam, J., Babu, P. D., Ranganathan, K., & Bindra, K. S. (2023). A study on effect of multiple laser shock peening on microstructure, residual stress, and mechanical strength of 2.5 Ni-Cr-Mo (EN25) low-alloy steel. *Journal of Materials Engineering and Performance*, *32*(10), 4361–4375. https://doi.org/10.1007/s11665-022-07402-2

[2] Wang, Q., Liu, X., Wang, W., Yang, C., Xiong, X., & Fang, H. (2017). Mixed mode fatigue crack growth behavior of Ni-Cr-Mo-V high strength steel weldments. *International Journal of Fatigue*, *102*, 79–91. https://doi.org/10.1016/j.ijfatigue.2017.05.001

[3] Wang, Q., Liu, X. S., Wang, P., Xiong, X., & Fang, H. Y. (2017). Numerical simulation of residual stress in 10Ni5CrMoV steel weldments. *Journal of Materials Processing Technology*, *240*, 77–86. https://doi.org/10.1016/j.jmatprotec.2016.09.011

[4] Wang, Q., Yan, Z., Liu, X., Dong, Z., & Fang, H. (2018). Understanding of fatigue crack growth behavior in welded joint of a new generation Ni-Cr-Mo-V high strength steel. *Engineering Fracture Mechanics*, *194*, 224–239. https://doi.org/10.1016/j.engfracmech.2018.03.016

[5] Wu, C., & Han, S. (2018). Microstructural evolution and mechanical properties of a low alloy high strength Ni-Cr-Mo-V steel during heat treatment process. *IOP Conference Series: Materials Science and Engineering*, *359*(1), 012027. https://doi.org/10.1088/1757-899X/359/1/012027

[6] Liu, X., Dong, Q., Wang, P., & Chen, H. (2021). Review of electron beam welding technology in space environment. *Optik*, *225*, 165720. https://doi.org/10.1016/j.ijleo.2020.165720

[7] Olshanskaya, T., Belenkiy, V., Fedoseeva, E., Koleva, E., & Trushnikov, D. (2020). Application of dynamic beam positioning for creating specified structures and properties of welded joints in electron-beam welding. *Materials*, *13*(10), 2233. https://doi.org/10.3390/ma13102233

[8] Schultz, H. (1993). *Electron beam welding*. UK: Woodhead Publishing.

[9] Arata, Y., Matsuda, F., & Nakata, K. (1972). Quench hardening and cracking in electron beam weld metal of carbon and low alloy hardenable steels. *Transactions of JWRI*, *1*(1), 39–51. https://doi.org/10.18910/8316

[10] Matsuda, F., & Ueyama, T. (1993). Solidification crack susceptibility of laser weld metal in 0.2C-Ni-Cr-Mo steels: Effects of bead configuration and S and P contents. *Welding International*, *7*(9), 686–692. https://doi.org/10.1080/09507119309548473

[11] Liu, S. D., Zhu, M. L., Zhou, H. B., Wan, D., & Xuan, F. Z. (2019). Strain visualization of growing short fatigue cracks in the heat-affected zone of a Ni-Cr-Mo-V steel welded joint: Intergranular cracking and crack closure. *International Journal of Pressure Vessels and Piping*, *178*, 103992. https://doi.org/10.1016/j.ijpvp.2019.103992

[12] Sisodia, R. P., & Gáspár, M. (2021). Experimental assessment of microstructure and mechanical properties of electron beam welded S960M high strength structural steel. *Manufacturing Letters*, *29*, 108–112. https://doi.org/10.1016/j.mfglet.2021.05.004

[13] Bai, Q., Ma, Y., Kang, X., Xing, S., & Chen, Z. (2017). Study on the welding continuous cooling transformation and weldability of SA508Gr4 steel for nuclear pressure vessels. *International Journal of Materials Research*, *108*(2), 99–107. https://doi.org/10.3139/146.111462

[14] Kar, J., Roy, S. K., & Roy, G. G. (2016). Effect of beam oscillation on electron beam welding of copper with AISI-304 stainless steel. *Journal of Materials Processing Technology*, *233*, 174–185. https://doi.org/10.1016/j.jmatprotec.2016.03.001

[15] Nayak, L. J., & Roy, G. G. (2021). Role of beam oscillation on electron beam welded zircaloy-4 butt joints. *Science and Technology of Welding and Joining*, *26*(6), 478–486. https://doi.org/10.1080/13621718.2021.1950498

[16] Wang, S., & Wu, X. (2012). Investigation on the microstructure and mechanical properties of Ti-6Al-4V alloy joints with electron beam welding. *Materials & Design (1980–2015)*, *36*, 663–670. https://doi.org/10.1016/j.matdes.2011.11.068

[17] Wang, X., Gong, X., & Chou, K. (2015). Scanning speed effect on mechanical properties of Ti-6Al-4V alloy processed by electron beam additive manufacturing. *Procedia Manufacturing*, *1*, 287–295. https://doi.org/10.1016/j.promfg.2015.09.026

[18] Doong, J. L., Chi, J. M., & Tan, Y. H. (1990). Fracture toughness behaviour in AISI 4130 steel of electron beam welding. *Engineering Fracture Mechanics*, *36*(6), 999–1006. https://doi.org/10.1016/0013-7944(90)90276-M

[19] Xia, X., Wu, J., Liu, Z., Shen, X., Ma, J., & Liu, Z. (2019). Study of microstructure difference properties of electron beam welds with beam oscillation of 50 mm 316L in CFETR. *Fusion Engineering and Design*, *138*, 339–346. https://doi.org/10.1016/j.fusengdes.2018.12.011

[20] Chen, Z., Loretto, M. H., & Cochrane, R. C. (1987). Nature of large precipitates in titanium-containing HSLA steels. *Materials Science and Technology*, *3*(10), 836–844. https://doi.org/10.1179/mst.1987.3.10.836

[21] Hsieh, K. C., Babu, S. S., Vitek, J. M., & David, S. A. (1996). Calculation of inclusion formation in low-alloy-steel welds. *Materials Science and Engineering: A*, *215*(1–2), 84–91. https://doi.org/10.1016/0921-5093(96)10370-1

[22] Sun, J., Zou, X., Matsuura, H., & Wang, C. (2018). Effect of heat input on inclusion evolution behavior in heat-affected zone of EH36 shipbuilding steel. *JOM*, *70*, 946–950. https://doi.org/10.1007/s11837-018-2824-1

[23] Wan, X., Zhou, B., Nune, K. C., Li, Y., Wu, K., & Li, G. (2017). In-situ microscopy study of grain refinement in the simulated heat-affected zone of high-strength low-alloy steel by TiN particle. *Science and Technology of Welding and Joining*, *22*(4), 343–352. https://doi.org/10.1080/13621718.2016.1242210

[24] Shim, J. H., Oh, Y. J., Suh, J. Y., Cho, Y. W., Shim, J. D., Byun, J. S., & Lee, D. N. (2001). Ferrite nucleation potency of non-metallic inclusions in medium carbon steels. *Acta*

Materialia, *49*(12), 2115–2122. https://doi.org/10.1016/S1359-6454(01)00134-3

[25] Vargas Cortés, V. H., Altamirano Guerrero, G., Mejía Granados, I., Baltazar Hernández, V. H., & Maldonado Zepeda, C. (2019). Effect of retained austenite and non-metallic inclusions on the mechanical properties of resistance spot welding nuggets of low-alloy TRIP steels. *Metals*, *9*(10), 1064. https://doi.org/10.3390/met9101064

[26] Venkatesh Kannan, M., Arivazhagan, N., Nageswara Rao, M., & Madhusudhan Reddy, G. (2020). Effect of inclusions on microstructure and mechanical behavior of multi-pass welded naval grade steel. *Proceedings of the Institution of Mechanical Engineers, Part L: Journal of Materials: Design and Applications*, *234*(8), 1071–1083. https://doi.org/10.1177/1464420720927727

[27] Wang, L., Gao, M., Zhang, C., & Zeng, X. (2016). Effect of beam oscillating pattern on weld characterization of laser welding of AA6061-T6 aluminum alloy. *Materials & Design*, *108*, 707–717. https://doi.org/10.1016/j.matdes.2016.07.053

[28] Singh, V., Srirangam, P., & Roy, G. G. (2023). Effect of beam oscillation on microstructure and mechanical properties of electron beam welded EN25 steel. *Materials*, *16*(7), 2717. https://doi.org/10.3390/ma16072717

[29] Biswas, S., Reddy, G. M., Mohandas, T., & Murthy, C. V. S. (2004). Residual stresses in Inconel 718 electron beam welds. *Journal of Materials Science*, *39*(22), 6813–6815. https://doi.org/10.1023/B:JMSC.0000045609.86430.19

[30] Cullity, B. D. (1956). *Elements of X-ray diffraction*. USA: Addison-Wesley Publishing.

[31] Mote, V. D., Purushotham, Y., & Dole, B. N. (2012). Williamson-Hall analysis in estimation of lattice strain in nanometer-sized ZnO particles. *Journal of Theoretical and Applied Physics*, *6*(1), 6. https://doi.org/10.1186/2251-7235-6-6

[32] Kalsoom, U. I., Bashir, S., & Ali, N. (2013). SEM, AFM, EDX and XRD analysis of laser ablated Ti in nonreactive and reactive ambient environments. *Surface and Coatings Technology*, *235*, 297–302. https://doi.org/10.1016/j.surfcoat.2013.07.056

[33] Sharma, S. K., Biswas, K., & Dutta Majumdar, J. (2021). Studies on electron beam surface remelted Inconel 718 superalloy. *Metals and Materials International*, *27*, 5360–5373. https://doi.org/10.1007/s12540-020-00884-6

[34] Neto, F. S., Neves, D., Silva, O. M. M., Lima, M. S. F., & Abdalla, A. J. (2015). An analysis of the mechanical behavior of AISI 4130 steel after TIG and laser welding process. *Procedia Engineering*, *114*, 181–188. https://doi.org/10.1016/j.proeng.2015.08.057

[35] Basak, S., Sharma, S. K., Mondal, M., Sahu, K. K., Gollapudi, S., Dutta Majumdar, J., & Hong, S. T. (2021). Electron beam surface treatment of 316L austenitic stainless steel: Improvements in hardness, wear, and corrosion resistance. *Metals and Materials International*, *27*, 953–961. https://doi.org/10.1007/s12540-020-00773-y

[36] Wang, Z., Oliveira, J. P., Zeng, Z., Bu, X., Peng, B., & Shao, X. (2019). Laser beam oscillating welding of 5A06 aluminum alloys: Microstructure, porosity and mechanical properties. *Optics & Laser Technology*, *111*, 58–65. https://doi.org/10.1016/j.optlastec.2018.09.036

[37] Yang, Z., & He, J. (2021). Numerical investigation on fluid transport phenomena in electron beam welding of aluminum alloy: Effect of the focus position and incident beam angle on the molten pool behavior. *International Journal of Thermal Sciences*, *164*, 106914. https://doi.org/10.1016/j.ijthermalsci.2021.106914

How to Cite: Singh, V., Roy, G. G., & Srirangam, P. (2024). Unveiling Impact of Electron Beam Optics on Weld Attributes in EN30B Steel. *Journal of Optics and Photonics Research*, *1*(3), 109–123. https://doi.org/10.47852/bonviewJOPR42021952